Student Dust Counter Status Report: The First 50 au

Edwin Bernardoni[1,2,3] , Mihály Horányi[1,2,3] , Alex Doner[1,2,3], Marcus Piquette[1,2,3], Jamey R. Szalay[4] , Andrew R. Poppe[5] ,
David James[2], Silvan Hunziker[6] , Veerle Sterken[6] , Peter Strub[7,8], Cathy Olkin[9] , Kelsi N. Singer[9] , John Spencer[9],
Alan Stern[9] , and Harold Weaver[10]

[1] Department of Physics, and Laboratory for Atmospheric and Space Physics, University of Colorado, Boulder, Boulder, CO 80302, USA
edwin.bernardoni@colorado.edu
[2] Laboratory for Atmospheric and Space Physics, University of Colorado, Boulder, CO 80303, USA
[3] NASA Solar System Exploration Research Virtual Institute (SSERVI): Institute for Modeling Plasmas, Atmospheres, and Cosmic Dust (IMPACT), CO 80301, USA
[4] Department of Astrophysical Sciences, Princeton University, Princeton, NJ 08544, USA
[5] Space Sciences Laboratory, University of California Berkeley, Berkeley, CA 94720, USA
[6] Institute for Particle Physics and Astrophysics, Zürich, Switzerland
[7] Max Planck Institute for Solar System Research, Göttingen, Germany
[8] Institute of Space Systems, University of Stuttgart, Germany
[9] Southwest Research Institute, Boulder, CO 80302, USA
[10] Johns Hopkins University Applied Physics Laboratory, Laurel, MD 20723-6099, USA
Received 2021 December 5; revised 2022 February 27; accepted 2022 March 2; published 2022 March 29

Abstract

The Venetia Burney Student Dust Counter (SDC) is an in situ dust detector on board the New Horizons spacecraft measuring the interplanetary dust particle (IDP) distribution for grains with mass $m > 10^{-12}$ g. SDC provides a near-continuous measure of the interplanetary dust environment, with recent results spanning beyond 50 au. This coverage includes the Edgeworth–Kuiper Belt (EKB), suggested by numerical models to be the dominant source of IDP in the outer solar system. Here we present the updated dust density distribution to 50 au and compare estimated flux values to existing theoretical models. SDC observes peak dust flux and densities near 42 au, and we expect a decay with increasing heliocentric distance. Based on SDC measurements, we also discuss the effects of IDP generation, transport, and loss on the evolution of the surfaces of EKB objects, the continual intermixing of their surface material, and the general tendency to homogenize their spectral properties. Continued SDC measurements remain critical for revealing the large-scale structure of the EKB and to guide the interpretation of dust disks around other stars. Additionally, we consider the potential of an interstellar dust (ISD) and "outer" Kuiper Belt contribution to SDC measurements and its effect on anticipated SDC flux values beyond 50 au, and we show that the inclusion of either source to the predicted model results in a noticeable deviation in anticipated SDC measurements beyond 50 au. Current and future SDC measurements also serve to constrain the relative contribution of ISD to SDC's flux and density estimates.

Unified Astronomy Thesaurus concepts: Interplanetary dust (821); Kuiper belt (893)

1. Introduction

Understanding of the dynamics of interplanetary dust particles (IDPs) provides key insight into the origin and evolution of planetary bodies within our solar system. The orbital evolution of IDPs is influenced by gravity due to the Sun and the planets, trapping in mean motion resonances (Liou et al. 1996; Moro-Martín & Malhotra 2002, 2003; Poppe 2016), radiation pressure, Poynting–Robertson (PR) drag, and electromagnetic forces, and their size distribution is altered by sublimation, sputtering, and mutual collisions (Vitense et al. 2012; Poppe 2016). In particular, Neptune tends to prolong the lifetime of IDPs born outside 30 au, while Jupiter blocks inward-flowing IDPs by ejecting most that cross its orbit. In general, IDPs flow toward the Sun, with production dominated by Edgeworth–Kuiper Belt object (EKBO) collisions in the outer solar system beyond Jupiter (Stern 1996; Yamamoto & Mukai 1998) and Jupiter Family Comet (JFC) outgassing dominating production in the inner solar system inside Jupiter's orbit (Nesvorný et al. 2010).

Several in situ dust detectors on various spacecraft have covered a broad range of the solar system. HEOS 2 and HELIOS observed the IDP environment near 1 au (Dietzel et al. 1973), while both Galileo and Ulysses measured from Earth to Jupiter, including measurements above/below the ecliptic plane (Krüger et al. 2019). Cassini observed IDPs between Jupiter and Saturn (Altobelli et al. 2007), while Pioneer 10 and 11 covered up to 9 and 18 au, respectively (Humes 1980). In addition to dedicated in situ dust detectors, Voyager measurements of approximately micron-sized dust particles were reported up to 100 au through the detection by radio and plasma wave instruments of the plasma clouds produced by impacts on the spacecraft (Gurnett et al. 1997).

The Venetia Burney Student Dust Counter (SDC) is an in situ dust detector aboard the New Horizons spacecraft, with IDP measurements spanning past 50 au to date for grains with mass $m > 10^{-12}$ g. Collisions between EKB objects are suggested by numerical models to be a dominant source of IDPs (Poppe 2016; Poppe et al. 2019). As such, measurements up to and beyond this range are key for resolving the validity of this prediction, which directly relates to the large-scale structure of our solar system and debris disks around other stars (Wyatt 2008). The results published here provide an updated look at this prediction, with additional measurements

in the near future expected to bring further clarification on the matter.

There are several effects of the dust production, transport, and loss of IDPs that can now be assessed based on SDC measurements. The characteristic speed between an IDP and EKBO is on the order of $1\text{--}4\ \text{km s}^{-1}$, resulting in, for example, the delivery of $\approx 4\ \text{kg day}^{-1}$ of water-bearing material into Pluto's atmospheres, altering its chemistry and contributing to the formation of haze layers (Poppe & Horányi 2018). These impact speeds are sufficient to generate secondary particles from airless icy EKBOs with nonnegligible yields, $Y = (\sum M_{\text{ejecta}})/M_{\text{primary}}$, in the range of 10–100 (Koschny & Grün 2001; Szalay et al. 2018). This yield range, however, remains somewhat uncertain, as the temperatures of icy surfaces in the outer solar system are much colder than those used in the laboratory experiments or expected to be on the lunar surface. Integrating over the IDP size and speed distributions reaching bare EKBO surfaces indicate a mass-loss rate in the range of $10^{-12}\text{--}10^{-11}\ \text{g m}^{-2}\ \text{s}^{-1}$, generating an ice erosion rate of $30\text{--}300\ \mu\text{m Myr}^{-1}$. Due to the fraction of low-speed impacts, the intermingling between the surface materials of separate EKBOs indicates a continual homogenization of their spectral properties (Seccull et al. 2021). The energy flux delivered by IDP impacts could also be relevant, fueling the phase transition between amorphous and crystalline ices (Porter et al. 2010).

With this in mind, we structure the publication as follows: Section 2 briefly reviews the layout and basic operation, as well as the long-term stability of SDC. In Section 3, we present the SDC measurements to date. Section 4 compares estimated IDP fluxes from these measurements to current theoretical models, with a brief discussion of changes from prior publications to the calculation of these fluxes. In Section 5, we assess the possible ISD contribution to the flux values, while Section 6 introduces a hypothetical "outer" Kuiper Belt structure and demonstrates its influence on future SDC flux measurements. Section 7 gives density estimates of IDPs in the EKB. Section 8 provides a summary of the work presented and a brief outlook for the expected results from continued SDC observations through the next decade (Stern et al. 2018). For SDC results up to and including New Horizons Pluto encounter, the reader is advised to consult prior publications (Poppe et al. 2010b; Han et al. 2011; Szalay et al. 2013; Piquette et al. 2019a).

2. SDC Instrument Description

SDC consists of an array of 14 impact sensors, permanently polarized polyvinylidene fluoride (PVDF) films, each with an area of $14.2\ \text{cm} \times 6.5\ \text{cm}$ and $28\ \mu\text{m}$ thick (Horányi et al. 2008). Dust impacts are measured from changes in the surface charge density due to cratering, a function of both the mass m and the impact speed v of the particle (Simpson & Tuzzolino 1985; James et al. 2010; Poppe et al. 2010a). The instrument is also sensitive to mechanical vibrations. For this reason, 12 panels reside on the exposed front, while the remaining 2 are unexposed to dust impacts on the underside and act as a means of noise characterization and mitigation during ground data processing. Additionally, panels are grouped into two separate rows with one reference channel each and record impacts through separate analog-to-digital converters (ADCs) labeled as sides A and B. These panels are mounted on a frame to the exterior of New Horizons facing the spacecraft's ram during nominal operation. Signals from the
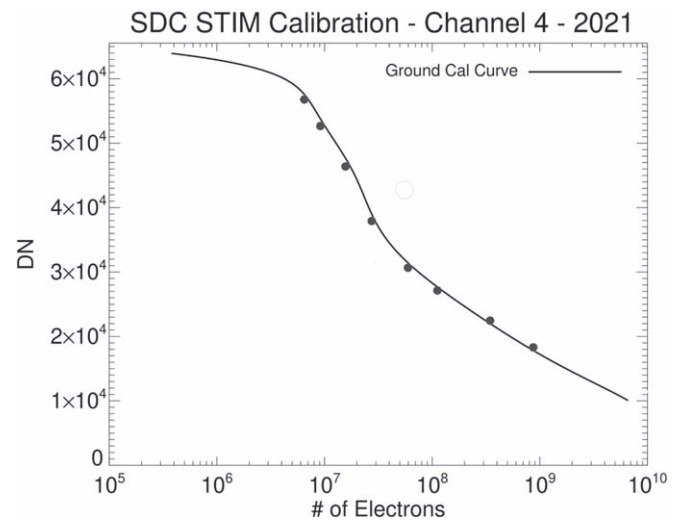

Figure 1. Stimulus tests are autonomously executed periodically throughout the mission and are compared to preflight calibration curves. An example of one such comparison is plotted for Channel 4. No aging effects of SDC's electronics are apparent to date.

panels are recorded by the instrument's electronic box within the spacecraft interior opposite the detector panels.

Electronic noise and possible instrument sensitivity degradation are monitored via periodic noise and charge stimulus tests. Noise tests consist of measuring all hits for each channel at thresholds initially far below operation values, followed by increasing steps in threshold value producing rates per threshold (Horányi et al. 2008). These noise tests are also used to determine threshold values for periods of high activity such as encounter flybys (Bagenal et al. 2016). Charge stimulus tests (Figure 1) are used to detect possible electronics degradation by injecting a known charge via a capacitor into each electronic chain. All channels are monitored and show minimal or no changes since launch. An in-depth analysis of relative channel sensitivities and differences between the A and B sides of the instrument is described comprehensively in the literature (Piquette et al. 2019a). For an updated look at noise events since 38 au, Figure 2 shows all events tagged as coincident within 1–10 s of either thruster firings, stimulus tests, or other recorded events. Note that the increase in coincident events beyond 33 au is due to mechanical vibrations from a waveguide switch corresponding to the spacecraft antenna, which has seen increased activity owing to down-linking of data. Similarly, recent changes in spacecraft operation have resulted in more frequent thruster firings for which SDC has remained on at higher thresholds, resulting in more coincident events with thruster firings.

For the purpose of ground data processing, calibrations from the 2 MV Van de Graaff dust accelerator at the Max Planck Institute for Nuclear Physics performed before launch are used with an assumed Keplerian IDP velocity modified by radiation pressure and added in quadrature with New Horizons velocity to convert the charge measurements to mass (Horányi et al. 2008; James et al. 2010). For this conversion, all dust grains are assumed to follow circular Keplerian, prograde orbits modified by radiation pressure. Valid hits (i.e., those excluding coincidences between channels or with spacecraft thruster firings) are used to produce flux and density estimates.
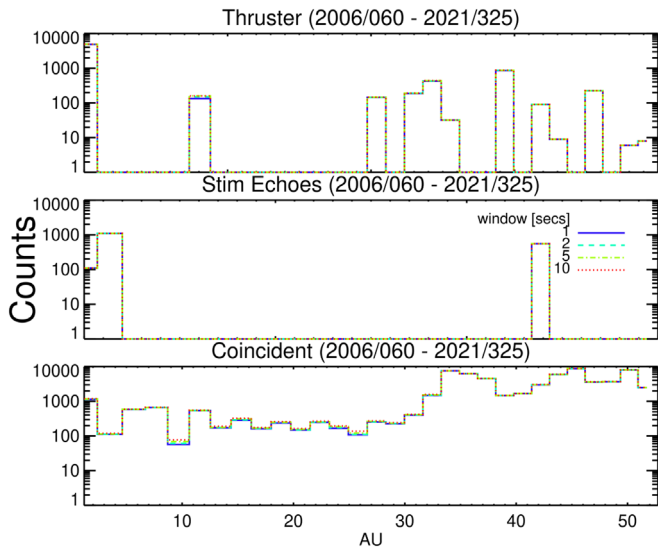
Figure 2. History of events tagged as noise due to coincidence with thruster firings (top), stimulus tests (middle), and other recorded events (bottom). Different line styles indicate the time window used for determining coincidence.

3. SDC Measurements out to 50 au

Figure 3 shows the trajectory of New Horizons to date, enabling a near-continuous measurement of the interplanetary dust environment by SDC to 50 au.

As each dust impact is detected as a single charge amplitude, this measure alone is not enough to distinguish real dust hits from piezoelectric or pyroelectric noise. To filter out such noise contributions, some measurements are flagged as "coincidence" during ground data processing. Hits that occur within a second of a thruster firing are most likely acoustic noise events. Similarly, hits on multiple channels at the same time are likely noise events, as the expected dust impact rate is approximately one hit per week; hence, such hits are likely due to mechanical vibrations from the spacecraft propagating through multiple panels.

Figure 4 shows all noncoincidence data as a function of heliocentric distance. As SDC measures impact charge, which is a function of both the mass and speed of the dust with respect to the instrument (Horányi et al. 2008; James et al. 2010; Poppe et al. 2010a; Piquette et al. 2019a, 2019b), a velocity and bulk mass density for the dust grain must be assumed to convert to mass. We use the standard silicate mass density for IDPs of 2.5 g cm^{-3}, with speeds derived from assuming circular Kepler orbits modified by radiation pressure for the dust grains. Missing segments in the coverage of Figure 4 are from either the instrument being off during those time periods for operational requirements or raised thresholds for all channels to allow SDC to remain turned on during active spacecraft operation, such as the Pluto and Arrokoth flybys. The rising minimum value in the mass with increasing distance is due to the spacecraft slowing down as it travels farther out of our solar system, raising the minimum detectable mass as shown in Figure 3.

To compare flux and density estimates as a function of distance and across all channels, a common mass cutoff threshold must be used. Due to the decrease in spacecraft speed, the cutoff thresholds used in this paper are larger than those in prior publications. We use a size cutoff for the IDP
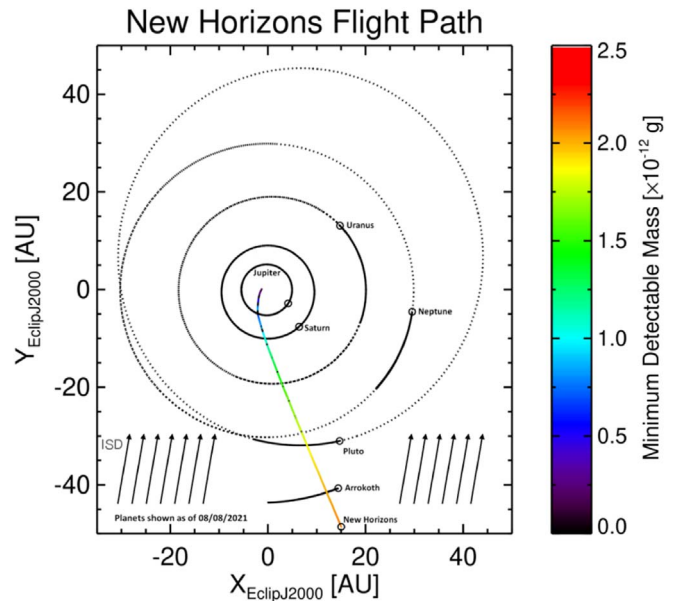

Figure 3. The trajectory of New Horizons past 50 au. The decrease in spacecraft speed with increasing distance results in a higher minimum detectable mass, clearly identified in the bottom panel of Figure 4. New Horizons is now heading along an ecliptic longitude $\lambda_{\text{NH}} = 293°$ compared to the ISD inflow of $\lambda_{\text{ISD}} \simeq 259°$, indicated by the parallel upward-pointing arrows at the bottom. Considering the magnitude of their speeds results in an impact angle of ISD onto SDC of $\alpha \simeq 23°$.
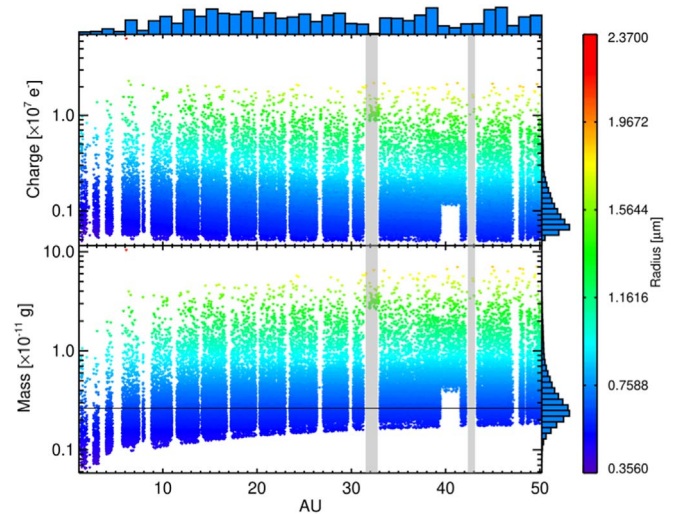

Figure 4. Plot of impact charges (top) and mass estimates (bottom) of all dust events recorded by SDC up to 50 au, excluding those flagged as coincidence events. Gray bars indicate Pluto and Arrokoth flybys, and a black horizontal line in the bottom plot indicates the 0.63 μm cutoff used for flux and density estimates, allowing for both A and B sides to contribute (Piquette et al. 2019b). Mass estimates assume silicate-dominated IDP grains with a density of 2.5 g cm^{-3} following circular Kepler orbits modified by radiation pressure. Histogram bars are included for both distance and charge/mass bins on their corresponding axes.

grain radius $r_g > 0.63 \mu$m to allow for all channels to contribute to the estimate given the decreasing spacecraft speed.

4. Flux Estimates

As each channel operates with varying thresholds and differing periods of operation time, the number of hits for science and reference channels are not directly comparable as a
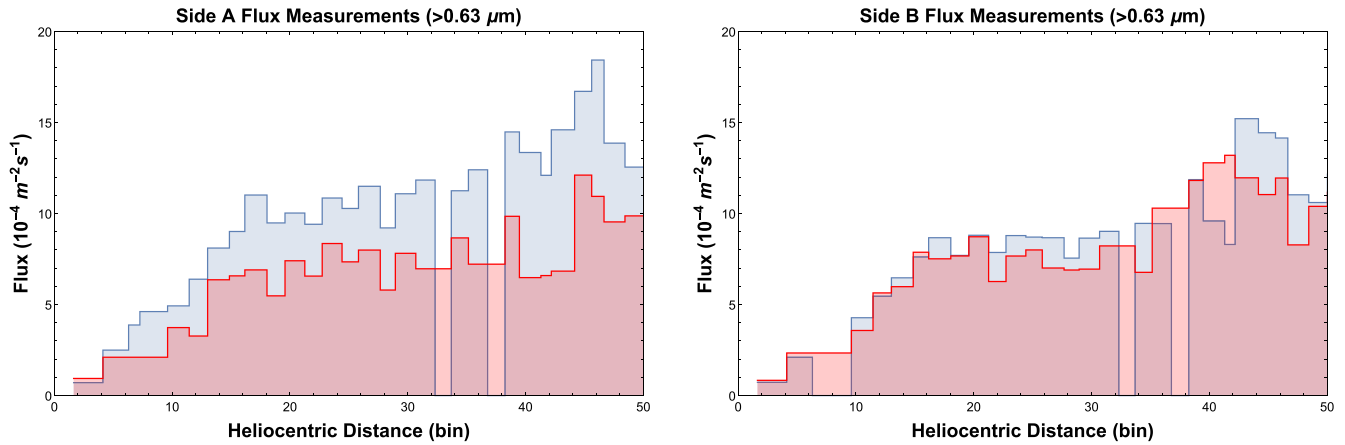
Figure 5. Plot of estimated dust flux average rates for all science channels (blue) compared to their corresponding reference channel (red) for electronic chain sides A (left) and B (right). While side B is noticeably less sensitive than side A, we currently have no means of definitively picking one side over the other as the "true" flux, and as such we continue with the average of the two. Note that the values plotted in Figure 6 are not simply the difference between the blue and the red, as the blue represents the mean of all science channel rates on that electronic chain. Instead, each science channel flux rate is individually reduced by the corresponding reference channel rate, with extra considerations outlined in Section 4.

measure of relative background noise. Instead, the estimated flux is used to account for these factors. For estimates of interplanetary dust flux onto SDC, we consider all noncoincidence data above a set size cutoff. Here we use a size cutoff for the IDP grain radius $r_g > 0.63\ \mu$m to allow for all channels to contribute to the estimate given the decreasing spacecraft speed discussed earlier. Counts are then binned in time or heliocentric distance, and rates are calculated per science panel with the following expression:

$$\tilde{r}_{si} = \frac{N_{si}}{dt_{si}} - \frac{N_{ri}}{dt_{ri}}, \qquad (1)$$

where N_{si} is the total valid counts on science channel i over the given bin and dt_{si} is the total valid "on" time for science channel i with thresholds below the given size cutoff. N_{ri} and dt_{ri} are the same respective quantities for the corresponding reference channel on the same electrical chain (A or B). Figure 5 plots the average of the science channel fluxes $\frac{N_{si}}{dt_{si}}$ in blue compared to their corresponding reference channel flux $\frac{N_{ri}}{dt_{ri}}$ for both electrical chains. While side B is noticeably less sensitive than side A, we currently have no means of definitively picking one side over the other as the "true" flux, and as such we continue with the average of the two for the following results. Errors and averages are calculated as the standard deviation and mean of this reduced rate per bin shown in Figure 6 for the size cutoff of IDP grain radius $r_g > 0.63\ \mu$m. Additionally, any channels for which their respective reference channel measured a higher rate were treated as having a reduced rate of zero for the purposes of averaging. Each channel was also required to cover a valid "on" time dt_{si} of at least 10% of the total time bin to be included in the average. Each electrical chain side (A or B) must additionally have more than one science channel to contribute.

It is important to note that these flux estimates differ slightly from the approach used in prior publications when it comes to determining the valid operation times as part of the initial rate calculation per channel. Previously, time bins were selected such that all channels were on with an appropriate cutoff threshold over the entire bin. Recent changes in SDC flight
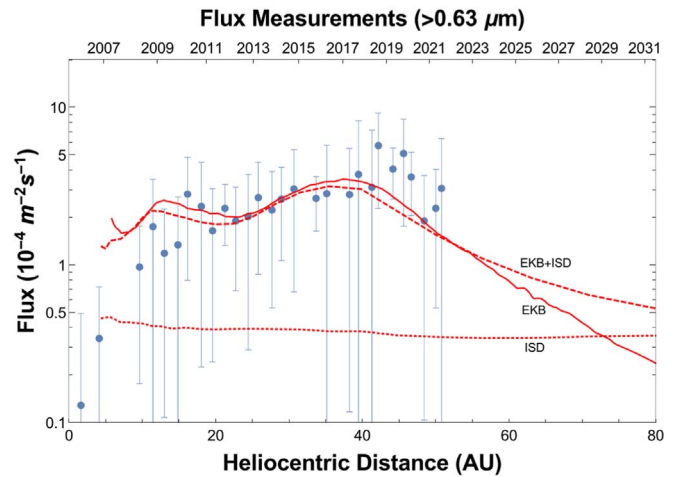

Figure 6. Plot of the estimated dust flux onto SDC for grains with IDP radii $>0.63\ \mu$m. The two red curves demonstrate the model given by Poppe (2016) and Poppe et al. (2019) fitted to SDC measurements assuming only IDP detections (solid curve) or an updated version assuming an additional ISD contribution (dashed curve), with the ISD component simulated with the IMEX model and the resulting ISD flux values calibrated using ISD measurements from Ulysses indicated by the horizontal dotted line (Sterken et al. 2015; Strub et al. 2019).

operation have resulted in frequent instrument threshold changes to allow for continued operation during frequent data downlinks and other activities. To account for this, we now use the new tracked threshold settings (labeled as "sdc_chn_lvl_dn.tab" in recent PDS data releases), combined with SDC on/off times to determine the total time that a channel is on and below the given mass cutoff threshold per time bin.

Plotted alongside flux estimates from SDC in Figure 6 are predictions from Poppe (2016) and Poppe et al. (2019) assuming only IDP detections (solid curve). The outer solar system's IDP distribution is dominated by production from mutual collisions (Stern 1996) and bombardment from interstellar and interplanetary dust (Yamamoto & Mukai 1998) of EKBOs. Beyond 42 au, the gradually decreasing trend in the fluxes as a function of distance could indicate that New Horizons has passed the peak density of the parent EKBO distribution, thereby approaching the outer edge of our dust

disk populated mainly by small particles forced onto eccentric orbits by radiation pressure effects (Krivov et al. 2006). The conversion from impact charge to mass, however, is appropriate for IDP only and must be revisited for the possible detection of interstellar dust (ISD) particles that flow through the solar system coincident with the flow of interstellar H and He with speeds $\simeq 26$ km s^{-1} (Grün et al. 1993; Frisch et al. 2009; McComas et al. 2012).

5. ISD Contribution

Due to the relative motion of the heliosphere with respect to the local interstellar medium, interstellar neutral atoms and dust particles (ISD) flow through our solar system with speeds $\simeq 26$ km s^{-1} (Frisch et al. 2009; McComas et al. 2012). The first in situ detection of ISD was made by Ulysses in 1992, during its encounter with Jupiter, sending the spacecraft on a solar polar orbit (Grün et al. 1993). Subsequently, Ulysses monitored the variability of the ISD flux for $\simeq 16$ yr, noticing strong temporal variability with solar cycle, reaching a maximum of $\simeq 1.8 \times 10^{-4}$ m^{-2} s^{-1} in 1992 and 2006 and a minimum of $\simeq 10^{-5}$ flux in 2000 (Strub et al. 2015). The mass of the vast majority of ISD detected by Ulysses was estimated to be 2.8×10^{-16} kg (or $\simeq 0.3$ μm with our assumed density of 2.5 g cm^{-3}), with diminishing contribution from larger or smaller particles (Landgraf et al. 2003; Krüger et al. 2015). Following the Ulysses discovery, the reanalysis of data from Helios and Galileo also identified ISD (Kruger et al. 2019; Altobelli et al. 2006; Baguhl et al. 1996; Altobelli et al. 2005, 2003). Cassini, in orbit around Saturn for $\simeq 13$ yr (of which $\simeq 10$ yr was used for the following estimate), recorded an average flux $\simeq 1.5 \times 10^{-4}$ m^{-2} s^{-1}, based on 36 ISD hits, also identifying their composition as magnesium-rich grains of silicate and oxide composition (Altobelli et al. 2016). The characteristic ISD size of $\simeq 0.3$ μm indicates that the ratio of radiation pressure over solar gravity $\beta \simeq 1$; hence, these grains would cross our solar system on approximately straight-line trajectories as shown in Figure 3. However, in addition to gravity and radiation pressure, dust particles in this size range also respond to electromagnetic forces, as they carry a positive charge and react on interplanetary magnetic fields, resulting in temporal variability of the ISD flux with solar cycle, alternating between periods of focusing toward and away from the ecliptic plane (Landgraf 2000; Sterken et al. 2012, 2015; Strub et al. 2019). While the basic interactions of ISD within the heliosphere appear to be well understood, our current models (calibrated using Ulysses data) can only reproduce the measurements of all spacecraft data of the variability of their flux measured to date within a factor of $2-3$ (Krüger et al. 2019). Hence, the question arises whether or not SDC detected ISD during its 15 yr cruise across the solar system.

SDC records dust particles through the charge amplitude they generate as a function of their impact speed v and mass m (Horányi et al. 2008; James et al. 2010; Piquette et al. 2020)

$$N_e \ [e] = 5.63 \times 10^{17} m [\mathrm{g}]^{1.3} v [\mathrm{km \ s}^{-1}]^{3.0}. \quad (2)$$

The traditional SDC analysis assumes that IDPs follow circular Kepler orbits modified by radiation pressure to calculate their impact speed. Hence, according to Equation (2), the much smaller and faster ISD will be assigned a larger IDP mass. With an expected size of 0.3 μm, speed of $\simeq 26$ km s^{-1}, and ecliptic longitude of $\lambda_{\mathrm{ISD}} \simeq 259°$ shown in Figure 3, we can predict
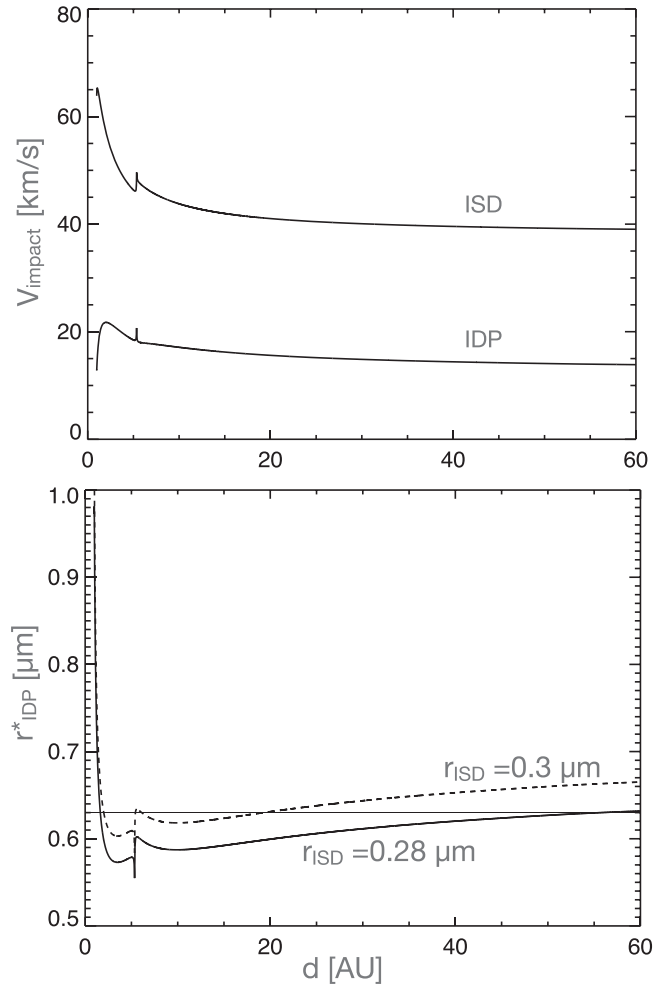

Figure 7. The impact speed of ISD and IDP (top) and the SDC pipeline's IDP size interpretation of 0.28 and 0.3 μm radius ISD impacts (bottom) as a function of heliocentric distance. Due to their higher speeds, ISD impacts on the detector panels are interpreted as larger-sized IDP detections as a result of the assumed dust velocity used in the conversion from charge to mass in Equation (2). Consequently, ISD is expected to contribute to SDC's flux estimates for the nominal IDP size cutoff of 0.68 μm indicated by the horizontal line.

what size SDC would mistake these ISD impacts as (Frisch et al. 2009; Landgraf et al. 2003; McComas et al. 2012; Krüger et al. 2015, 2019). The top panel of Figure 7 shows the anticipated impact speed of a 0.3 μm ISD compared to the assumed speed used in the IDP conversion from charge to mass in Figure 4. From the charge produced for a 0.3 μm ISD with its expected impact speed converted to size using the assumed IDP speed, we produce the SDC pipeline's size interpretation of ISD impacts as a function of heliocentric distance, shown in the bottom panel of Figure 7. The typical 0.3 μm ISD grain is interpreted as larger than 0.63 μm for most of SDC's current coverage and thus should contribute at our current mass cutoff threshold.

This detectability, however, is quite close to the cutoff threshold, with only a size difference of 0.02 μm pushing nominal ISD detectability below the cutoff threshold. As mentioned previously, the 0.3 μm estimate was done using data primarily from the defocusing phase of the solar cycle, and thus the nominal ISD size is likely smaller. For this reason, we

present two model fits in Figure 6 for the purpose of comparing with SDC flux measurements. For one case (solid curve), we assume only IDP detections following the model given by Poppe (2016) and Poppe et al. (2019) (i.e., the ISD contribution is just below the IDP size cutoff of 0.63 μm). For the second case (dashed curve), an additional ISD component (dotted line) was simulated with the IMEX model (Sterken et al. 2015; Strub et al. 2019) and the resulting ISD flux values calibrated using Ulysses ISD measurements. In particular, Figure 1 in Strub et al. (2019) and Figures 3 and 4 in Sterken et al. (2015) are crucial for the reader trying to understand the ISD models as they are now. The potential contribution of ISD should become increasingly apparent with additional detections beyond 50 au, particularly beyond 73 au, where the expected EKB contribution becomes comparable to the ISD contribution, as indicated by the divergence in the two model fits in Figure 6. When extrapolating to measurements beyond 50 au, we should also consider the potential for the presence of an additional "outer" Kuiper Belt separate from the "main" EKB known to date (Petit et al. 2011).

6. OKB Contribution

As a test case, we consider a putative outer Kuiper Belt (referred to hereafter as the OKB to distinguish from the main EKB) consisting of a population of objects between 80 and 110 au on circular orbits with low to moderate inclinations (majority of objects <30°). While yet to be observed, an OKB may be an important source of IDPs via either mutual collisions (Stern 1996; Abedin et al. 2021) or ISD grain bombardment (Yamamoto & Mukai 1998). Thus, signatures of the OKB may be observable to in situ dust instruments such as New Horizons/SDC.

To predict the structure and observability of a putative OKB dust disk, we simulated dust grains originating from the parent OKB body distribution and compared the resulting dust distribution to those grains previously simulated for the main EKB (Han et al. 2011; Poppe 2016; Poppe et al. 2019). Given the uncertain nature of the OKB parent object observations, our initial model for the OKB dust disk is simplified in several ways. First, we have only run grains with radii 0.5, 0.7, 1.0, 1.5, and 2.0 μm, as these are the main contributors to the SDC impact count rate. Between 250 and 400 individual grains were modeled at each of the five size bins, giving moderately good statistics for the OKB population compared to previous work (1200 grains per size bin were modeled for each size bin in the EKB population as described in Poppe 2016). Second, we have not included the effects of grain–grain collisions on the OKB grains, as the collisional algorithm requires simulated grains up to the 500 μm size (Poppe 2016). Based on the results of applying the collisional algorithm to similar, small IDP grains from the main EKB, we expect only minor deviations since the PR drag time for such small grains is shorter than their typical collisional lifetime (see Figure 10 of Koschny et al. 2019). Third, our initial conditions for the dust grain orbital elements are estimated as semimajor axes between 80 and 110 au (uniformly distributed), eccentricities less than 0.25, and inclinations less than 15°. The longitude of ascending node, argument of perihelion, and true anomaly are all uniformly drawn from [0, 2π]. Fourth, the possible effects of neutral interstellar gas pressure on the IDP dynamics (Scherer 2000) are not considered in the present study, but identified as an avenue for future investigation for outer solar system dust
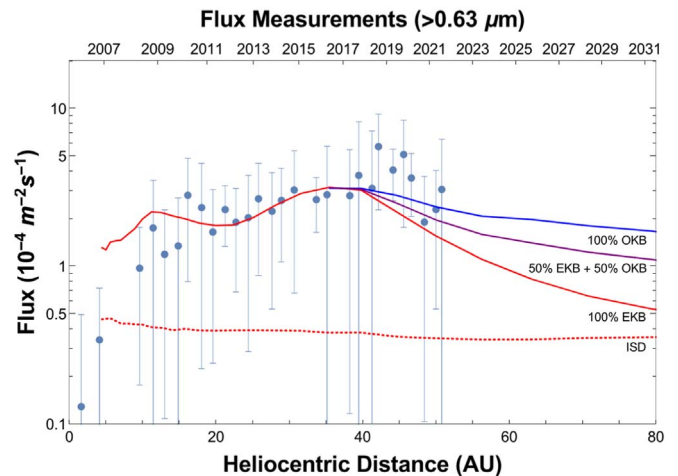

Figure 8. Plot of the estimated dust flux onto SDC for grains with IDP radii >0.63 μm. The three curves demonstrate the model given by Poppe (2016) and Poppe et al. (2019) fitted to SDC measurements assuming only an EKB distribution (red), a putative OKB distribution with initial semimajor axes between 80 and 110 au (blue), and a combination of the two with equal weight (purple). All three include an ISD contribution (dotted line) as in Figure 6.

dynamics. Finally, the dust production rate from the OKB is not known a priori; thus, we compare several cases for the relative EKB and OKB production rates that are nevertheless consistent with SDC measurements to date (Piquette et al. 2019a).

With the requirement that a predicted combination of fluxes to SDC from EKB and OKB sources must be consistent with previous SDC measurements, we plot three modeled SDC flux combinations as a function of heliocentric distance in Figure 8, each with the inclusion of the ISD estimate (dotted line) discussed in Section 5. The EKB-only case (red) corresponds to our previous understanding of the extent of the Kuiper Belt from Petit et al. (2011), which generally had few objects >50 au (with the exception of the scattered/outer disk). The predicted flux to SDC peaks at 10 au (outside the Saturn/Jupiter gravitational barriers) and at 30–40 au in the main EKB belt. At distances greater than 40 au, the flux to SDC declines steadily and approaches the "background" ISD flux level. In comparison, the half-EKB/half-OKB and OKB-only cases show an extension in the SDC impact fluxes beyond 50 au. Total predicted fluxes to SDC in these cases are approximately 50%–100% larger than in the EKB-only case for the 60–80 au region. Note that the predicted EKB and OKB fluxes to SDC in the 50–100 au range are significantly higher than those predicted for Oort Cloud cometary (OCC) grains (see Figure 1(b) of Poppe et al. 2019). We note that the SDC impact rates do not reach a local maximum in the 80–110 au region. This is due to several factors, including the "kick" in orbital parameters to newly born dust grains when they first are subjected to radiation pressure, the relatively rapid decay in eccentricity and semimajor axis due to PR drag, and the lack of relatively strong mean motion resonances in the 80–110 au region that would temporarily halt the inward progression of dust grains (as is seen in the 30–40 au region). It may be possible that larger-sized grains, whose PR drag lifetimes are shorter than their collisional lifetimes, may yield spatial distributions that peak in the 80–110 au region; however, SDC is not likely to observe such large grains owing to their very low spatial densities. Nevertheless, continued SDC measurements at distances >50 au will allow for constraints
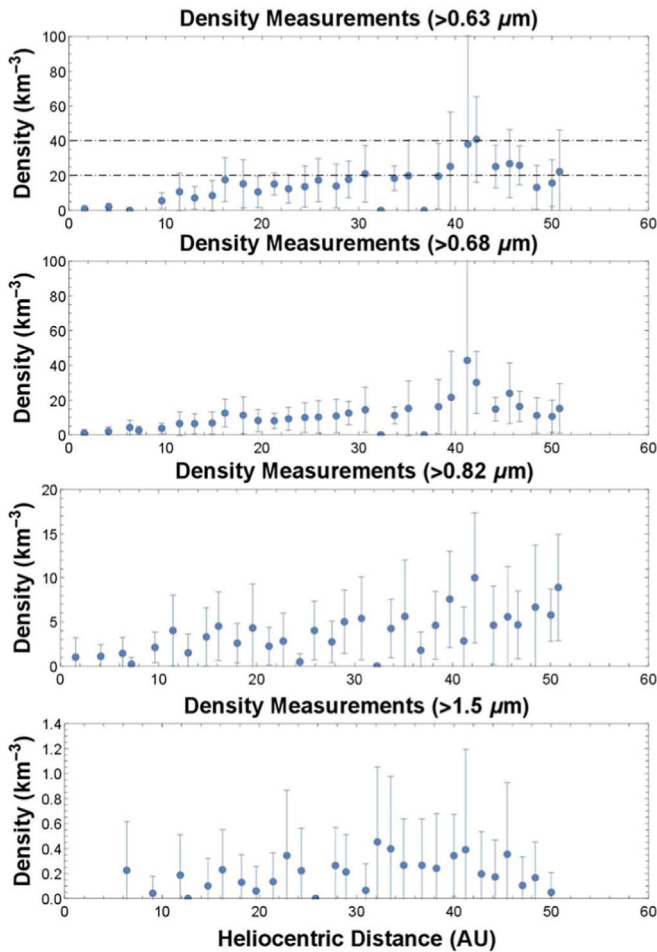
Figure 9. Plot of estimated IDP density for grains with radii $>0.63\,\mu$m (top), $>0.68\,\mu$m (second), $>0.82\,\mu$m (third), and $>1.5\,\mu$m (bottom) as measured by SDC. Note that these estimates are upper limits on the IDP density, as the contribution from ISD impacts is not removed. However, ISD impacts are not expected to contribute for thresholds above 0.68 μm. Voyager estimates from plasma wave data are indicated by dashed lines in the top panel. Points plotted at 0 with no error bars are empty bins from containing either no valid detections for any panel or no valid time coverage for any panel within that time period.

on the possible presence and production rate of any putative OKB distribution.

7. Density Estimates

For SDC estimates of interplanetary dust densities, we continue with the same valid time selection scheme used for the flux estimates. We now require additional velocity information for determining the volume sampled per detector panel for each valid time range

$$V = A_{\rm det} \int_{T_1}^{T_2} \hat{\boldsymbol{n}}_{\rm SDC}(\boldsymbol{v}_{\rm sc} - \boldsymbol{v}_{\rm dust})dt, \qquad (3)$$

where T_1 and T_2 are the start and stop times of one valid time segment within the temporal bin, respectively. The total volume over the entire temporal bin is then a sum of all such segments. $A_{\rm det}$ is the area of a single detector panel, $\hat{\boldsymbol{n}}_{\rm SDC}$ is the surface normal of the detector panel, $\boldsymbol{v}_{\rm sc}$ is New Horizon's velocity vector, and $\boldsymbol{v}_{\rm dust}$ is the dust velocity vector assuming circular Kepler velocities modified by radiation pressure. In the same manner as the flux estimates, each science panel's density
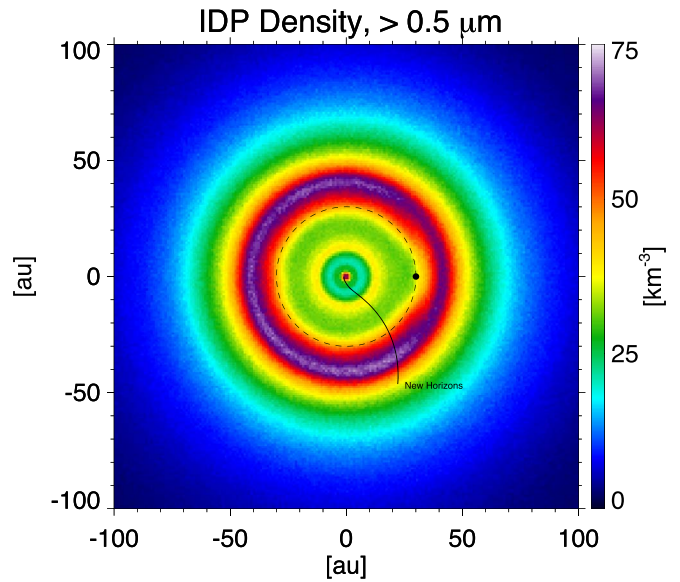

Figure 10. The total modeled IDP density in the Neptune-rotated frame. The dotted and dashed lines denote the position and orbit of Neptune, respectively, while the solid line denotes the trajectory of the New Horizons spacecraft.

estimate is reduced by its respective reference channel and averaged with errors calculated as the standard deviation across all contributing channels. Any channels for which their respective reference channel measured a higher density were again treated as having a reduced density of zero for the purposes of averaging. Figure 9 shows IDP density estimates at four size cutoffs: 0.63, 0.68 0.82, and 1.5 μm. The 0.63 μm cutoff corresponds to the minimum cutoff allowed for all panels to contribute to the estimate in the last time bin, while the 0.68 μm cutoff corresponds to the minimum cutoff to remove the expected ISD contribution derived from Figure 7. The 0.82 μm comes from the same consideration but for "medium" threshold settings, while 1.5 μm is derived from the threshold settings used during the Pluto and Arrokoth flybys and three-axis periods. For dust grains with radii $>0.63\,\mu$m, the density demonstrates an increase up to and through the Kuiper Belt. Comparing this to the 20–40 km^{-3} estimated by the Voyager spacecraft shows a reasonable agreement with SDC observations (Gurnett et al. 1997, 2015). Note, however, that while the quoted size threshold for this estimate is $\sim$1 μm, the mass-to-charge conversion factor can vary by up to a factor of 10, leading to a possible size threshold of $\sim$0.5–2.3 μm (Gurnett et al. 1997). For this reason, we include the estimate in the 0.63 μm size cutoff of Figure 9, though the thresholds between the two may sightly differ.

Figure 10 shows the total modeled interplanetary dust densities in the ecliptic plane, in a Neptune-rotated frame, summed over all three dust sources (EKB, OCC, and JFC) and all sizes (0.5–500 μm radius), with total production rates for EKB, OCC, and JFC dust grains from Poppe et al. (2019). The dotted and dashed lines at 30 au denote the position and orbit of Neptune, respectively. Local maxima in the density are found (i) within 1 au from combined EKB and JFC contributions undergoing PR drag into the inner heliosphere, (ii) near 10 au from EKB grains trapped in mean motion resonance with both Saturn and Jupiter, and (iii) centered on 40 au from direct production from EKBO and trapping in mean motion

resonance with Neptune. The peak density in the EKB reaches approximately 75 km^{-3} for all grains >0.5 μm, while the peak density for those grains >0.63 μm (i.e., the SDC minimum detectable size used here) is approximately 35 km^{-3}, commensurate with the SDC data shown in Figure 5. Under the assumption that there is not an additional distant component to the EKB beyond what is currently anticipated (Petit et al. 2011), the total IDP densities at 50 and 100 au gradually decline to 45 and 5 km^{-3}, respectively.

8. Summary

With New Horizons passing 50 au, we now have direct measurements of the IDP environment from SDC through most of the Kuiper Belt. Under the assumption of circular Kepler orbits for the dust grains, we present mass distribution measurements, estimates for the IDP flux to SDC, and density as a function of distance from the Sun. For dust grains with $r_g > 0.63$ μm, SDC flux estimates approaching the OKB seem to follow our latest models (Poppe 2016; Poppe et al. 2019), which are based on dust production from the currently anticipated parent EKB distribution (Petit et al. 2011).

While we anticipate that ISD should contribute to SDC flux values as shown by Figure 7, this contribution should become increasingly apparent beyond 50 au as New Horizons leaves the EKBO-generated IDP distribution (see Figure 6). A potential OKB would also produce diverging flux estimates for the 60–80 au region depending on the relative dust production to EKB-sourced IDPs as shown in Figure 8. These estimates, however, are based on a hypothetical OKB for the purpose of quantifying how such a structure would influence SDC flux values beyond 50 au. Density estimates for dust grains with $r_g > 0.63$ μm remain consistent with Voyager estimates (Gurnett et al. 1997).

The New Horizons spacecraft is healthy and could continue operating through the 2030s, reaching a heliocentric distance of 90−100 au. SDC will continue its measurements of the interplanetary dust fluxes in the outer solar system, detecting the collisional debris of the parent EKBOs.

SDC observations into the *terra incognita* ≫ 50 au will provide an unparalleled opportunity to learn about the large-scale structure of the EKB, constrain the upwind ISD fluxes, and offer unique insights into the interpretation of telescopic observations of dust disks around other stars.

ORCID iDs

Edwin Bernardoni https://orcid.org/0000-0002-6191-3028
Mihály Horányi https://orcid.org/0000-0002-5920-9226
Jamey R. Szalay https://orcid.org/0000-0003-2685-9801
Andrew R. Poppe https://orcid.org/0000-0001-8137-8176
Silvan Hunziker https://orcid.org/0000-0003-2021-4535
Veerle Sterken https://orcid.org/0000-0003-0843-7912
Cathy Olkin https://orcid.org/0000-0002-5846-716X
Kelsi N. Singer https://orcid.org/0000-0003-3045-8445
Alan Stern https://orcid.org/0000-0001-5018-7537
Harold Weaver https://orcid.org/0000-0003-0951-7762

References

Abedin, A. Y., Kavelaars, J. J., Greenstreet, S., et al. 2021, AJ, 161, 195
Altobelli, N., Dikarev, V., Kempf, S., et al. 2007, JGRA, 112, 7105
Altobelli, N., Grün, E., & Landgraf, M. 2006, A&A, 448, 243
Altobelli, N., Kempf, S., Krüger, H., et al. 2005, JGRA, 110, A07102
Altobelli, N., Kempf, S., Landgraf, M., et al. 2003, JGRA, 108, 8032
Altobelli, N., Postberg, F., Fiege, K., et al. 2016, Sci, 352, 312
Bagenal, F., Horányi, M., McComas, D. J., et al. 2016, Sci, 351, aad9045
Baguhl, M., Grün, E., & Landgraf, M. 1996, SSRv, 78, 165
Dietzel, H., Eichhorn, G., Fechtig, H., et al. 1973, JPhE, 6, 209
Frisch, P. C., Bzowski, M., Grün, E., et al. 2009, SSRv, 146, 235
Grün, E., Zook, H., Baguhl, M., et al. 1993, Natur, 362, 428
Gurnett, D. A., Ansher, J. A., Kurth, W. S., & Granroth, L. J. 1997, GeoRL, 24, 3125
Gurnett, D. A., Persoon, A. M., Granroth, L., & Kurth, W. S. 2015, AGUFM, 2015, SH53C–06
Han, D., Poppe, A. R., Piquette, M., Grün, E., & Horányi, M. 2011, GeoRL, 38, 24102
Horányi, M., Hoxie, V., James, D., et al. 2008, SSRv, 140, 387
Humes, D. H. 1980, JGR, 85, 5841
James, D., Hoxie, V., & Horányi, M. 2010, RScI, 81, 034501
Koschny, D., & Grün, E. 2001, Icar, 154, 391
Koschny, D., Soja, R. H., Engrand, C., et al. 2019, SSRv, 215, 34
Krivov, A. V., Löhne, T., & Sremčević, M. 2006, A&A, 455, 509
Krüger, H., Strub, P., Altobelli, N., et al. 2019, A&A, 626, A37
Krüger, H., Strub, P., Grün, E., & Sterken, V. J. 2015, ApJ, 812, 139
Kruger, H., Strub, P., Srama, R., et al. 2019, P&SS, 172, 22
Landgraf, M. 2000, JGR, 105, 10303
Landgraf, M., Krüger, H., Altobelli, N., & Grün, E. 2003, JGRA, 108, 8030
Liou, J.-C., Zook, H. A., & Dermott, S. F. 1996, Icar, 124, 429
McComas, D. J., Dayeh, M. A., Allegrini, F., et al. 2012, ApJS, 203, 1
Moro-Martín, A., & Malhotra, R. 2002, AJ, 124, 2305
Moro-Martín, A., & Malhotra, R. 2003, AJ, 125, 2255
Nesvorný, D., Jenniskens, P., Levison, H. F., et al. 2010, ApJ, 713, 816
Petit, J.-M., Kavelaars, J. J., Gladman, B. J., et al. 2011, AJ, 142, 131
Piquette, M., James, D., & Horányi, M. 2020, RScI, 91, 023307
Piquette, M., Poppe, A. R., Bernardoni, E., et al. 2019a, Icar, 321, 116
Piquette, M. R., James, D., & Horanyi, M. 2019b, AGUFM, 2019, P33I–3534
Poppe, A., Jacobsmeyer, B., James, D., & Horányi, M. 2010a, NIMPA, 622, 583
Poppe, A., James, D., Jacobsmeyer, B., & Horányi, M. 2010b, GeoRL, 37, 11101
Poppe, A. R. 2016, Icar, 264, 369
Poppe, A. R., & Horányi, M. 2018, A&A, 617, L5
Poppe, A. R., Lisse, C. M., Piquette, M., et al. 2019, ApJL, 881, L12
Porter, S., Desch, S., & Cook, J. 2010, Icar, 208, 492
Scherer, K. 2000, JGR, 105, 10329
Seccull, T., Fraser, W. C., & Puzia, T. H. 2021, PSJ, 2, 57
Simpson, J. A., & Tuzzolino, A. J. 1985, NIMPA, 236, 187
Sterken, V. J., Altobelli, N., Kempf, S., et al. 2012, A&A, 538, A102
Sterken, V. J., Strub, P., Krüger, H., von Steiger, R., & Frisch, P. 2015, ApJ, 812, 141
Stern, S. A. 1996, A&A, 310, 999
Stern, S. A., Weaver, H. A., Spencer, J. R., & Elliott, H. A. 2018, SSRv, 214, 77
Strub, P., Krüger, H., & Sterken, V. J. 2015, ApJ, 812, 140
Strub, P., Sterken, V. J., Soja, R., et al. 2019, A&A, 621, A54
Szalay, J. R., Piquette, M., & Horányi, M. 2013, EP&S, 65, 1145
Szalay, J. R., Poppe, A. R., Agarwal, J., et al. 2018, SSRv, 214, 98
Vitense, C., Krivov, A. V., Kobayashi, H., & Löhne, T. 2012, A&A, 540, A30
Wyatt, M. C. 2008, ARA&A, 46, 339
Yamamoto, S., & Mukai, T. 1998, A&A, 329, 785